Enhancing the crystallinity and perfecting the orientation of formamidinium tin iodide for highly efficient Sn-based perovskite solar cells

Shao, Shuyan; Dong, Jingjin; Duim, Herman; ten Brink, Gert H.; Blake, Graeme R.; Portale, Giuseppe; Loi, Maria Antonietta

Published in:
Nano energy

DOI:
10.1016/j.nanoen.2019.04.040

Publication date:
2019

Nano Energy 60 (2019) 810–816

Contents lists available at ScienceDirect

Nano Energy

journal homepage: www.elsevier.com/locate/nanoen

Communication

Enhancing the crystallinity and perfecting the orientation of formamidinium tin iodide for highly efficient Sn-based perovskite solar cells

Shuyan Shao, Jingjin Dong, Herman Duim, Gert H. ten Brink, Graeme R. Blake, Giuseppe Portale, Maria Antonietta Loi*

Zernike Institute for Advanced Materials, University of Groningen, Nijenborgh 4, 9747 AG, Groningen, the Netherlands

ARTICLE INFO

Keywords:
Lead-free perovskite solar cells
Trap assisted recombination
Tin vacancies
Crystallinity
Orientation

ABSTRACT

Low power conversion efficiency (PCE) and poor reproducibility are among the main challenges for tin-based perovskite solar cells (HPSCs). The facile formation of tin vacancies and oxidation of the divalent tin cation during the thin film fabrication process are among the causes of these problems, because the tin perovskite layer then becomes p-doped, resulting in significant trap-assisted recombination losses in devices. In this paper, we demonstrate that increasing the crystallinity of the tin perovskite film is an effective way to address the open issues with Sn-based perovskites. We succeed in improving the crystallinity of the 3D formamidinium tin iodide ($FASnI_3$) grains, increasing their size, and perfecting their orientation in the out-of-plane direction by incorporating ethylammonium iodide (EAI) into a 2D/3D tin perovskite film (where 2D is $PEA_2FASn_2I_7$, PEA = phenylethylammonium). This leads to a decrease of traps and background charge carrier density, and therefore to decreased charge recombination losses in EA_x2D/3D based devices, as compared not only to devices based on $FASnI_3$ but also to those based on 2D/3D mixtures. As a consequence, devices using a perovskite layer with composition $EA_{0.08}$2D/3D exhibit much higher PCE (8.4%) and better reproducibility compared to devices based on mixed 2D/3D perovskites (7.7%) and 3D perovskite (4.7%).

1. Introduction

Organic lead halide perovskite-based solar cells (HPSCs) have achieved a certified power conversion efficiency (PCE) of 23.7% by the beginning of 2019 [1]. Such an astonishing achievement is unprecedented in the history of photovoltaic technology [2]. This high efficiency is a result of intensive efforts to optimize the device structure, interfacial layers and the perovskite thin film structure and composition [3–13]. A more fundamental reason for this success lies in the perovskites' excellent optical and electrical properties such as high absorption coefficient, tunable absorption spectrum, very low exciton binding energy, small hole and electron effective masses, good charge transport and high charge carrier diffusion length. Despite these excellent properties and the high efficiency achieved, there are still many concerns about the large-scale application of these solar cells because they contain water soluble, toxic Pb^{2+}.

The most straightforward manner to address this issue is to find a benign or less toxic metal to replace the lead atom in the perovskite structure, while retaining the excellent optical and electrical properties of the Pb-based materials. Recent theoretical studies suggest that the $6s^26p^0$ electronic configuration of Pb^{2+} creates a shallow conduction band edge and small hole and electron effective masses, which are responsible for the unique optoelectronic properties of the lead-based perovskites. Therefore, metals with a ns^2np^2 electronic configuration are good candidates to replace lead in the perovskite structure [14,15].

Sn is among the most promising candidates to replace Pb as they both belong to the IVA group and have isoelectronic configurations. Tin-based perovskites hold promise to produce similar or even higher PCE than their Pb-based counterparts, benefiting from broader absorption and higher charge carrier mobility [15–17]. However, tin-based perovskites have thus far not exhibited the same rapid increase in PCE as their Pb-based counterparts. For a relatively long time (about three years) the best PCE reported for tin-based HPSCs was lower than 7% despite intensive research efforts devoted to tuning the composition, device structure, deposition methods and film morphology [8,18–22].

The facile formation of tin vacancies and easy oxidation of Sn^{2+} have been identified as the main reasons for the low PCE and the poor reproducibility of this kind of solar cells. The mechanism can briefly be described as a large degree of charge carrier recombination losses in the

* Corresponding author.
E-mail address: m.a.loi@rug.nl (M.A. Loi).

https://doi.org/10.1016/j.nanoen.2019.04.040
Received 6 March 2019; Received in revised form 1 April 2019; Accepted 8 April 2019
Available online 10 April 2019

solar cells due to the high level of self-p-doping and high background charge carrier density in the Sn-based active material [23,24]. The fabrication of tin HPSCs therefore has very strict requirements. The processing atmosphere needs to be clean with very low water and oxygen levels. In addition, the ultrahigh purity of the Sn source materials such as SnI_2 is of paramount importance for the performance of the solar cells [23,25]. However, it is challenging to obtain ultrapure tin iodide with good reproducibility as this requires both the synthesis and purification to be performed in strictly oxygen-free atmosphere, which leads to high production costs. For example, SnI_2 with a purity of 99.999% costs twice that of 99.99% purity.

We have recently demonstrated that a small amount of 2D ($PEA_2FASn_2I_7$) tin perovskite templates the growth of highly crystalline and oriented 3D $FASnI_3$ grains. This 2D/3D mixture effectively suppresses the formation of tin vacancies and Sn^{2+} oxidation [23]. As a consequence of the reduced background charge carrier density and trap-assisted charge recombination, this device showed a 50% improvement in PCE compared to the use of pure 3D tin perovskite as the light absorber. Nevertheless, the introduction of larger amounts of bulky ligands, which gives rise to the formation of 2D perovskites, creates pinholes in the film and limits further improvement in the device performance. Hsu et al. demonstrated that using ethylammonium iodide (EAI) as additive significantly improve the crystallinity of the lead-based 3D perovskite films as well as the device performance [26]. So far, there has been no reports on using EAI as additive in tin based HPSCs.

Herein, we succeed in reducing the number of defects in the 2D/3D tin perovskite film by adding EAI to the corresponding perovskite precursor solution (hereafter referred to as EA_x2D/3D). We find that the EA cation is incorporated in the crystal structure of the 3D perovskite ($FASnI_3$), inducing a further crystallization of the 3D $FASnI_3$ grains with the pseudo-cubic axis in the out-of-plane direction. As a consequence, EA_x2D/3D samples exhibit superior crystallinity and stronger orientation compared to the 2D/3D films. Moreover, EA_x2D/3D films display more uniform film morphology compared to their counterparts without the EA cation. These features lead to a much reduced trap and background charge carrier density, which induce a reduction in charge recombination losses. These features explain the enhanced overall performance and reproducibility of the EA_x2D/3D devices compared to their 2D/3D counterparts.

2. Experimental details

2.1. Materials

Poly(3,4-ethylenedioxythiophene):polystyrene sulfonate (PEDOT:PSS) water dispersion (Clevios VP AI 4083) was acquired from Heraeus. 2-phenylethylammonium iodide (PEAI, > 98%) and formamidinium iodide (FAI, > 98%) were purchased from TCI EUROPE N.V. SnI_2 (99.99%), tin fluoride (SnF_2) (> 99%), fullerene (C_{60}, > 99.9%), 2,9-dimethyl-4,7-diphenyl-1,10-phenanthroline (BCP, 99.99%), dimethylformamide (DMF, 99.8%) and dimethyl sulfoxide (DMSO, 99.8%) were purchased from Sigma Aldrich.

2.2. Thin film characterization

SEM images were recorded in vacuum using a FEI NovaNano SEM 650 with an acceleration voltage of 5 kV. XRD patterns of the perovskite films were recorded on a Bruker D8 Advance X-ray diffractometer with a Cu Kα source (λ = 1.54 Å) and a Lynxeye detector. Grazing incidence wide-angle X-ray scattering (GIWAXS) measurements were performed using a MINA X-ray scattering instrument built on a Cu rotating anode source (λ = 1.5413 Å). 2D patterns were collected using a Vantec500 detector (1024 × 1024 pixel array with pixel size 136 × 136 μm) located 93 mm away from the sample. The perovskite films were placed in reflection geometry at certain incident angles α_I with respect to the direct beam using a Huber goniometer. GIWAXS patterns were acquired using incident angle of 2° in order to probe the thin film structure at aX-ray penetration depth of the entire film thickness. For an ideally flat surface, the value of the X-ray penetration depth (i.e. the depth into the material measured along the surface normal where the intensity of X-rays falls to 1/e of its value at the surface) depends on the X-ray energy (wavelength λ), the critical angle of total reflection, α_c, and the incident angle, α_i, and can be estimated using the relation: $\Lambda = \frac{\lambda}{4\pi}\sqrt{\frac{2}{(\alpha_i^2-\alpha_c^2)^2+4\beta^2-(\alpha_i^2-\alpha_c^2)}}$, where β is the imaginary part of the complex refractive index of the compound. The estimated X-ray penetration depth is about 350 nm at an incident angle of 2.0° for the tin perovskite samples. For this calculation, densities of 3.56 g/cm^3 were used for these samples. The direct beam center position on the detector and the sample-to-detector distance were calibrated using the diffraction rings from standard silver behenate and Al_2O_3 powders. All the necessary corrections for the GIWAXS geometry were applied to the raw patterns using the FIT2D and the GIXGUI Matlab toolbox. The reshaped GIWAXS patterns, taking into account the inaccessible part in reciprocal space (wedge-shaped corrected patterns), are presented as a function of the vertical and parallel scattering vectors q_z and q_r. The scattering vector coordinates for the GIWAXS geometry are given by:

$$3.\ q = \begin{cases} q_x = \frac{2\pi}{\lambda}(\cos(2\theta_f)\cos(\alpha_f) - \cos(\alpha_i)) \\ q_y = \frac{2\pi}{\lambda}(\sin(2\theta_f)\cos(\alpha_f)) \\ q_z = \frac{2\pi}{\lambda}(\sin(\alpha_i) + \sin(\alpha_f)) \end{cases}$$

where $2\theta_f$ is the scattering angle in the horizontal direction and α_f is the exit angle in the vertical direction. The parallel component of the scattering vector is thus calculated as $q_r = \sqrt{q_x^2 + q_y^2}$.

Time-resolved photoluminescence (PL) measurements were conducted by exciting the samples with the second harmonic (400 nm) of a mode-locked Ti:Sapphire femtosecond laser (Mira 900, Coherent). The repetition rate of the laser is 76 MHz; a pulse picker was inserted in the optical path to decrease the repetition rate of the laser pulses. The laser power (0.76 μJ cm^{-2}) was adjusted using neutral density filters. The excitation beam was focused with a 150-mm focal length lens, and the emission was collected and coupled into a spectrometer with a 50 lines/mm grating. Time-resolved measurements were performed using a Hamamatsu streak camera operating in single-sweep mode. The capacitance-voltage (*C-V*) measurements were conducted under dark condition at a frequency of 10 KHz with an ac driving voltage of 20 mV and DC bias in the range of −0.6 to 0.6 V on a Solarton 1260 impedance gain-phase analyzer. UV–Vis spectra of the perovskite films were recorded on Shimatzu UV-Vis-NIR spectrophotometer (UV 3600).

2.3. Device fabrication

ITO glasses were cleaned using an ultra-sonication bath in soap water and rinsed sequentially with de-ionized water, acetone and isopropyl alcohol. A PEDOT:PSS layer was then spin-coated onto the ITO substrates at 4000 rpm for 60 s and dried at 140 °C for 20 min. The coated substrates were then transferred to a nitrogen-filled glove-box to spin-coat the tin perovskite film. The 2D/3D film was obtained from a precursor solution comprising 0.08 M PEAI, 0.92 M FAI, 1 M SnI_2 and 0.1 M SnF_2 in mixed solvents of DMSO and DMF (1:4 vol ratio) at 4000 rpm for 60s. Diethyl ether was used as the anti-solvent during the spin-coating process. The EA_x2D/3D tin perovskite films were obtained under the same conditions from solutions containing x M EAI (x = 0.08 M, 0.12 M, 0.16 M), 0.08 M PEAI, 0.92 M FAI, 1 M SnI_2, and 0.1 M SnF_2. On top of the perovskite active layer, 60 nm C_{60}, 6 nm BCP and 100 nm Al layers were sequentially evaporated under vacuum (< 10^{-6} mbar). The J-V curves of the perovskite solar cells were measured at 295 K in a nitrogen-filled glove box under simulated AM

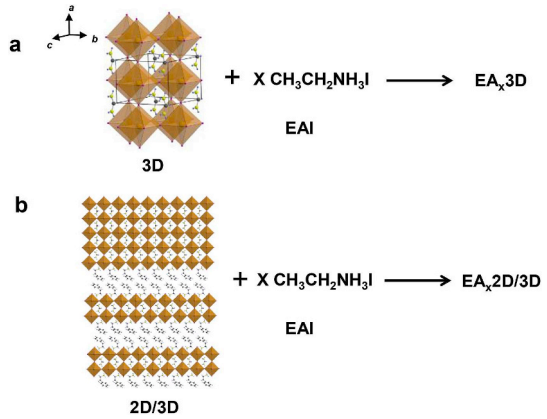

Fig. 1. Schematic illustration of the (a) EA_x3D and (b) $EA_x2D/3D$ samples.

1.5 G solar illumination obtained with a Steuernagel Solar constant 1200 metal halide lamp with a Keithley 2400 source meter. The light intensity was calibrated to be 100 mW cm^{-2} by using a Si reference cell and correcting for the spectral mismatch. A shadow mask (0.04 cm^2) was used to exclude lateral contributions beyond the device area.

3. Results and discussion

We firstly prepared EA_x3D and $EA_x2D/3D$ films by adding specific amounts of EAI in the 3D and 2D/3D precursor solutions, in which 0.1 M SnF_2 was used as reducing agent (see Fig. 1). It is worth mentioning that SnI_2 with lower purity (99.99%) was used in this work to reduce the production costs, in contrast to our previous work where precursors of 99.999% purity were used.[18] We then recorded x-ray diffraction (XRD) patterns of these samples to examine the effects of the EA cation on the crystal structure and grains of the 3D $FASnI_3$ (Fig. 2). Using randomly oriented $FASnI_3$ powder obtained from crushed single crystals as a reference sample, the most obvious change with increasing EA content is an increasing degree of orientation of $FASnI_3$ along the pseudo-cubic {100} direction (Fig. 2a and c). Moreover, these EA_x3D samples exhibit significantly higher crystallinity compared to the pure 3D sample as demonstrated by the sharp increase in intensity of the 100 and 200 peaks, along with the reduction in the peak full-width-at-half-maximum (FWHM) (Table S1). For clarity, we compared the intensity and FWHM of the 100 peak for different samples (Fig. S1), which shows a clear trend (narrowing and increasing intensity) with increasing EA concentration. The incorporation of EA cations into the 2D/3D sample thus enhances the crystallinity of the 3D grains.

The XRD patterns indicate that the same crystal structure is retained for all the samples. We notice that the EA_x3D and $EA_x2D/3D$ samples have a slight expansion in the unit cell parameters (Table S1), as evidenced by the shift of the *h*00 diffraction peaks towards lower diffraction angles (Fig. 2b and d). This could be caused by the incorporation of the larger EA cation into the 3D crystal structure. A more careful inspection of the XRD patterns reveals that at least two additional peaks at $2\theta \approx 12.65^\circ$ (d ≈ 7.01 Å) and $2\theta \approx 25.45^\circ$ (d ≈ 3.50 Å) appear and grow with increasing EA content. A possible impurity with a unit cell that would give peaks at these positions is SnI_4 (cubic, space group Pa-3, lattice parameter 12.268 Å). This impurity might appear due to the formation of a "hollow" perovskite structure where the bulky EA cation replaces the entire tin iodide octahedra. A similar trend was observed in the $EA_x2D/3D$ samples. Recently Ke et al. demonstrated that the incorporation of ethylenediammonium into a 3D film also gave a small increase in unit cell volume, and they speculated that tin iodide octahedra are removed to accommodate the bulkier ethylenediammonium cation in the 3D structure.[19] However, in those ethylenediammonium substituted tin perovskite films no significant impurity phase was observed in the XRD patterns, and there was no significant preferred orientation or improvement in the crystallinity of the perovskite phase either.[19] These results are in contrast to what we observe in the EA-substituted 3D and 2D/3D samples in this work.

We further performed grazing incidence wide-angle x-ray scattering (GIWAXS) measurements to assess the effects of EA cation on the structure and orientation of the $FASnI_3$ crystals with respect to the substrate. Fig. 3 shows the GIWAXS patterns of the 2D/3D, $EA_{0.08}3D$, and $EA_{0.08}2D/3D$ perovskite films recorded at an incident angle of 2°, which allows x-ray to penetrate the entire film thickness. Recently, we have demonstrated that the pure 3D film has significant randomness in the orientations of the grains throughout the entire film thickness,[18] while the 2D/3D film exhibits preferential orientation of the 3D grains

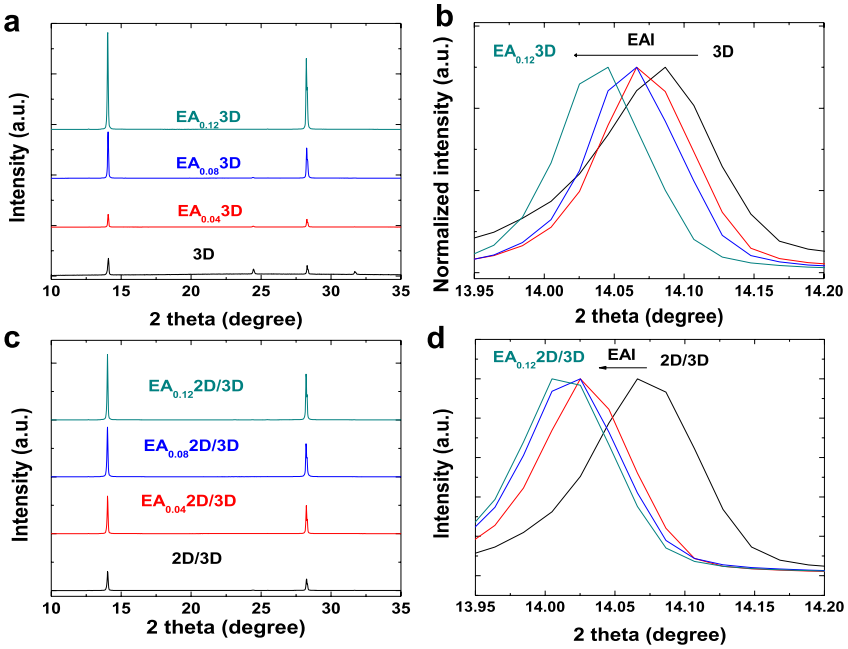

Fig. 2. XRD patterns of (a) and (b) EA_x3D films; (c) and (d) $EA_x2D/3D$ films (x = 0, black line; 0.04, red line; 0.08, blue line; 0.12, dark cyan line). Note: For clarity, the diffraction intensity of the pure 3D sample is magnified by 20 times.

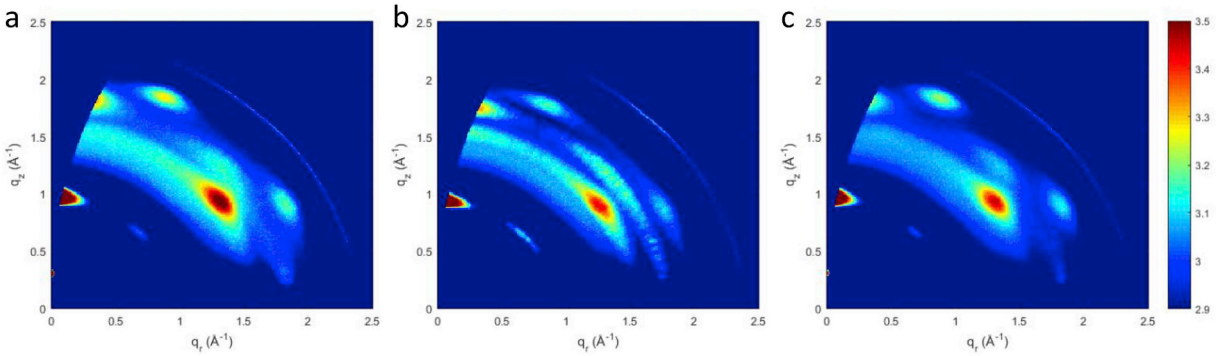

Fig. 3. GIWAXS patterns for the (a) 2D/3D sample, (b) $EA_{0.08}$3D sample, and (c) $EA_{0.08}$2D/3D sample. The patterns were recorded using an incident angle of 2°.

with {*h*00} planes parallel to the substrate, i.e. the pseudo-cubic axis is oriented perpendicular to the substrate throughout the entire film thickness.[18] The $EA_{0.08}$3D sample investigated here (Fig. 3b) also exhibits Bragg spots at similar positions to the 2D/3D sample (Fig. 3a), indicating the same preferential orientation of the grains with respect to the substrate. Compared to the $EA_{0.08}$3D and 2D/3D samples, the $EA_{0.08}$2D/3D sample (Fig. 3c) displays better defined Bragg spots, indicating stronger orientation and more perfect packing of the {*h*00} planes in the out-of-plane direction.

Since the morphology of the perovskite film is critical for the device performance, we performed scanning electron microscopy (SEM) measurements to examine the effects of the EA cation on the morphology of the films (Fig. 4). The pure 3D film exhibits non-compact morphology with quite a few pinholes, which creates a high concentration of structural defects such as dangling bonds and vacancies. In tin perovskite films, tin vacancies are the dominant defects due to their small formation energy. Therefore, those pinholes could serve as non-radiative recombination centers causing significant trap-assisted recombination. Moreover, the pinholes are likely to give rise to shunts in solar cells due to the direct contact of the cathode and anode interfacial materials, producing severe leakage currents. The addition of the EA cation effectively eliminates the pinholes and induces the formation of larger grains in the 3D film, which reduces the quantity of defects in the perovskite film. The same effect of adding the EA cation was also observed in the $EA_{0.08}$2D/3D sample. These observations are in line with the improved crystallinity and larger grains indicated by the XRD patterns of the $EA_{0.08}$3D and $EA_{0.08}$2D/3D films.

The above discussion of the crystallographic and morphological changes of the tin perovskite films in the presence of the EA cation indicates the potential benefits of using such films as the light absorber layer in solar cells. To verify this, we fabricated devices with the configuration ITO/poly(3,4-ethylenedioxythiophene):polystyrene sulfonate (PEDOT:PSS)/perovskite film/C_{60}/2,9-dimethyl-4,7-diphenyl-1,10-phenanthroline (BCP)/Al following the procedure reported in our previous work [23].

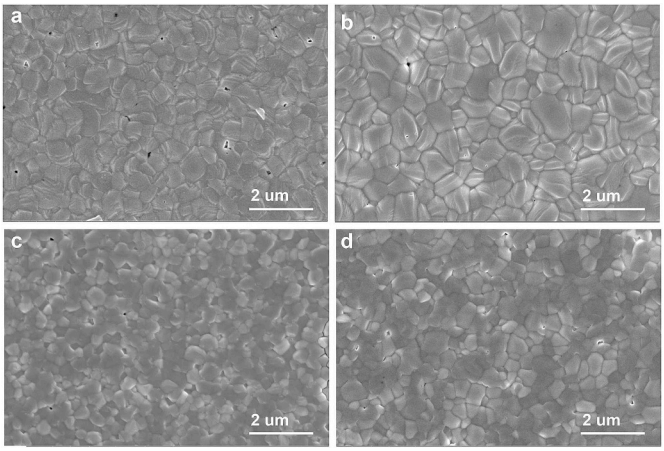

Fig. 4. SEM images of (a) 3D, (b) $EA_{0.08}$3D, (c) 2D/3D, and (d) $EA_{0.08}$2D/3D samples.

In the aforementioned recent work we demonstrated superior device performance using mixed 2D/3D perovskites as the light absorbing layer, rather than pure 3D tin perovskite.[18] Here we proved this trend once gain (Fig. S3). Therefore, we used the mixed 2D/3D perovskite as a model system in the present work and investigated the effects of the EA concentration on the performance of EA_x2D/3D-based solar cells (Fig. S3). Compared to devices using pure 2D/3D films, EA_x2D/3D films yield obvious improvement in the overall device performance, such as a higher open circuit voltage (V_{OC}), short circuit current density (J_{SC}), fill factor (FF) and power conversion efficiency (PCE). Devices using EA_x2D/3D as the active layer have relatively constant device performance with initially increasing EA concentration, which then drops for concentrations higher than 0.12 M. The drop in PCE is mainly due to a decrease in photocurrent density. Since the charge transport occurs in the 3D corner-sharing network of tin iodide octahedra, the formation of octahedron vacancies where the EA cations are located inhibits their effective electronic coupling and deteriorates the charge transport. Moreover, the presence of a high EA concentration is also detrimental to the optical absorption spectrum of EA_x2D/3D (x = 0.16), in which the absorption onset and bandgap emission are shifted towards shorter wavelength (Fig. S4). These factors collectively reduce the photocurrent density.

Fig. 5a shows the current density (*J*)-voltage (*V*) characteristics under one sun illumination of the best performing solar cells using 2D/3D and $EA_{0.08}$2D/3D tin based perovskite films. The device using the 2D/3D film displays a V_{OC} of 0.48/0.49 V, a J_{sc} of 23.25/23.33 mA cm^{-2}, a FF of 0.68/0.67 and a PCE of 7.61%/7.70% at forward/reverse sweep. It is important to underline that these numbers are slightly lower than those we reported earlier.[18] One of the possible reasons, as mentioned above, is the lower quality of the SnI_2 (99.99%) in the present work than what was used in our previous work (99.999%). Another possible factor contributing to the lower PCE is the batch to batch variation in the quality of the interfacial materials (C60 and BCP).

The incorporation of EA cations into the 2D/3D film significantly improves the overall performance of the solar cells, which display a V_{OC} of 0.51/0.51 V, a J_{SC} of 23.75/23.60 (mA cm^{-2}), a FF of 0.70/0.69, and a PCE of 8.40%/8.31% at forward/reverse sweep. We list all these parameters and figures of merit in Table 1. It is worth mentioning that the $EA_{0.08}$2D/3D-based device shows very small hysteresis, which is clearly seen from the negligible changes in the J-V curves for forward/reverse scans and varied sweeping rates (Fig. 5b). A negligible hysteresis in the J-V curves is critical to achieve reliable device performance. To confirm our observation, we tested the steady state PCE of this device, which remained stable at 7.87% for over 700s (Fig. 5c). The

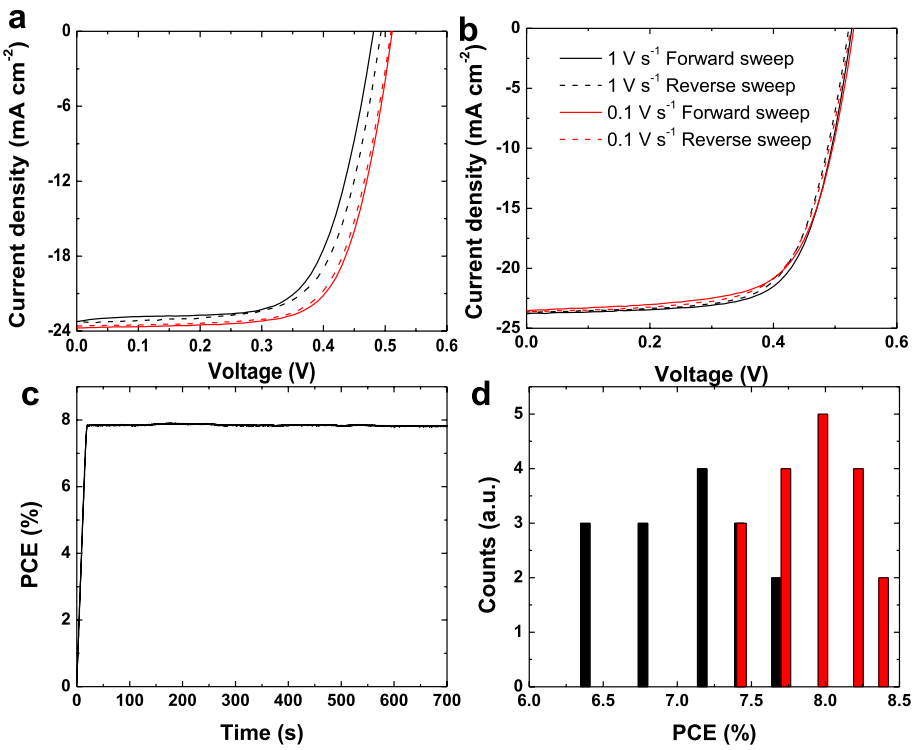

Fig. 5. (a) J-V curves of the champion devices based on 2D/3D (black) and $EA_{0.08}$2D/3D-based solar cells (red) under one sun AM 1.5 G condition. (b) Forward and reverse sweeps of the J-V characteristics of the champion solar cell based on $EA_{0.08}$2D/3D measured at different rates. (c) Steady-state PCE tracked at the maximum power point of the device based on $EA_{0.08}$2D/3D. (d) Histogram of the distribution of PCE for devices based on the 2D/3D (black) and $EA_{0.08}$2D/3D samples (red).

Table 1
Figures of merit for devices with 2D/3D and $EA_{0.08}$2D/3D tin perovskite layers under one sun condition.

Device	V_{OC} (V)	J_{SC} (mA cm^{-2})	FF	PCE (%)
2D/3D	F 0.48	23.25	0.68	7.61
	R 0.49	23.33	0.67	7.70
$EA_{0.08}$2D/3D	F 0.51	23.75	0.70	8.40
	R 0.51	23.60	0.69	8.31

incident photon to electron conversion efficiency (IPCE) spectrum confirms the improvement in the J_{SC} of the device using $EA_{0.08}$2D/3D (Fig. S5). Moreover, the integrated photocurrent values are in good agreement with the measured J_{SC}s from the J-V test. To compare the reproducibility of devices using 2D/3D and $EA_{0.08}$2D/3D films, we fabricated more than 12 devices of each type. Fig. 5d shows the PCE statistics obtained for these devices. The devices based on $EA_{0.08}$2D/3D films show a much narrower distribution of PCEs compared to devices based on pure 2D/3D mixtures. This higher reproducibility is obviously a very important advantage of this new composition.

Revealing the charge recombination process in these solar cells is the key to understanding the origin of the improvement in device performance (higher PCE and better reproducibility). As mentioned above, polycrystalline tin perovskite films suffer from high self-p-doping (background holes) due to the low formation energy of tin vacancies, which act as electronic traps. To check how the background charge carrier density changes in tin perovskite films with and without EA cations, we recorded the capacitance (C) of the corresponding devices under dark conditions. The background charge carrier density was extracted from the slope of the linear region of the C^{-2} vs V plot in Fig. 6a by using Mott-Schottky analysis,

$$C^{-2} = \frac{2}{q\varepsilon_r\varepsilon_0 N}\left(V - V_{fb} - \frac{kT}{q}\right)$$

The device based on $EA_{0.08}$2D/3D has a hole carrier density of $2.0 \times 10^{16}\,cm^{-3}$, which is about half of that in the 2D/3D-based solar cell ($4.37 \times 10^{16}\,cm^{-3}$). This reduction in the background hole carrier density indicates a reduced number of electronic trap states in the $EA_{0.08}$2D/3D film.

A consequence of the high density of background holes is that the charge carrier recombination dynamics is dominated by the monomolecular recombination mechanism determined by the non-radiative recombination of the photo-generated electrons with the background holes, when the excitation intensity is equal to or lower than one sun illumination,. [16,27]. This also means that monomolecular recombination dominates the performance of tin-based HPSCs under one sun illumination.

Fig. 6b shows time-resolved photoluminescence (PL) data for the 2D/3D and $EA_{0.08}$2D/3D samples, measured with the aim of studying the effects of the EA cation on the decay dynamics of the charge carriers. For these experiments an excitation intensity of lower than one sun was used. The 2D/3D film exhibits much faster decay of the photogenerated carriers and has a shorter emission lifetime of 8.9 ns due to the capture of free carriers by defect sites and the subsequent monomolecular recombination of these carriers. Here it is important to underline that this is a much longer lifetime compared to the 4.3 ns measured earlier on $FASnI_3$.[18] The $EA_{0.08}$2D/3D sample has a much longer emission lifetime of 16 ns, confirming the lower trap density and lower degree of non-radiative trap-assisted recombination losses. Therefore, we can conclude that the more ordered crystal structure and the reduced density of grain boundaries indeed gives rise to a much lower trap density in these Sn-based perovskite films.

With knowledge of the mechanism of charge recombination in the perovskite thin films, it is also important to gain more insight into the charge recombination rate in the operating solar cells. For this purpose, we performed impedance spectroscopy measurements under one sun illumination at open circuit condition on the devices using 2D/3D and $EA_{0.08}$2D/3D films. The impedance spectra were fitted by the equivalent model consisting of series resistance R_1, a constant phase element (CPE) and recombination resistance R_2 as shown in the inset of Fig. 6c. The characteristic lifetime τ of the charge carriers in the devices was extracted from the product of the recombination resistance (R_2) and the chemical capacitance ($C_2 = Q_2(2\pi f_{peak})^{a-1}$), where f_{peak} is the peak frequency of the Nyquist plot, a indicates the deviation from an ideal

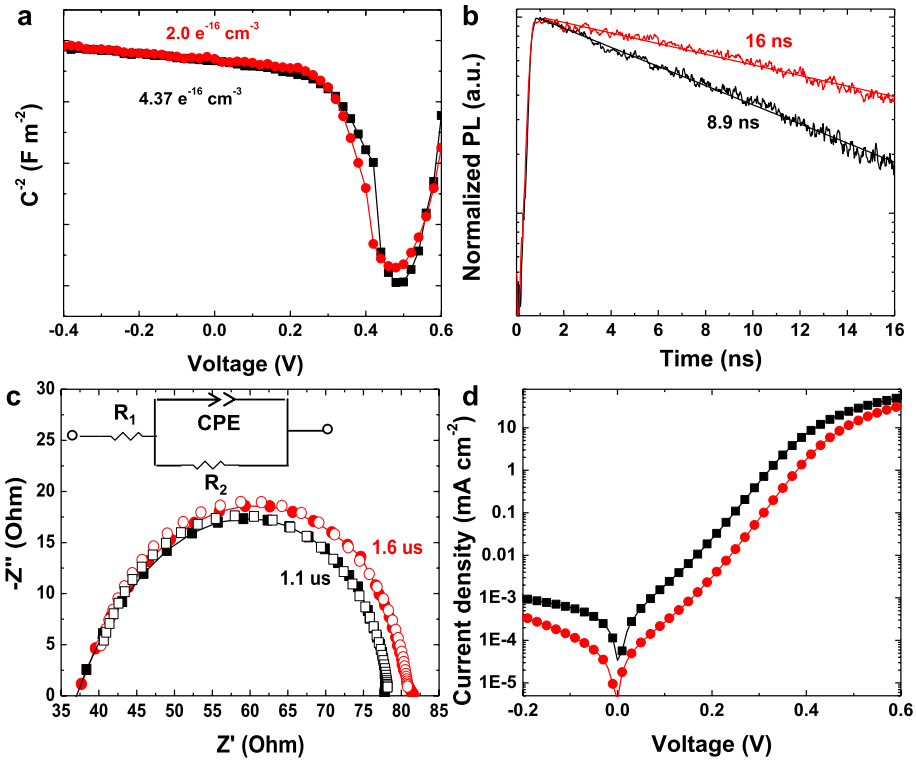

Fig. 6. (a) C^{-2} as a function of bias voltage of the devices based on 2D/3D (black squares) and $EA_{0.08}$2D/3D (red circles) perovskite films. (b) Time-resolved PL for 2D/3D (black line) and $EA_{0.08}$2D/3D (red line) perovskite films. (c) Impedance spectra of devices based on 2D/3D (black squares) and $EA_{0.08}$2D/3D (red circles) perovskite films measured under one sun illumination at open circuit condition. (d) J-V curves under dark condition for devices based on 2D/3D (black squares) and $EA_{0.08}$2D/3D (red circles) perovskite layers.

capacitor, and Q is the CPE parameter. The photo-generated free charge carriers in the 2D/3D based device have a lifetime of about 1.1 μs, while those in the $EA_{0.08}$2D/3D-based device have a longer lifetime of 1.6 μs. These results further verify that the charge recombination is slowed down in the $EA_{0.08}$2D/3D-based device due to the suppressed charge recombination associated with the background doping and traps. Fig. 6d shows the dark *J-V* curves of the devices based on 2D/3D and $EA_{0.08}$2D/3D tin perovskite films. The $EA_{0.08}$2D/3D-based solar cell has a much lower leakage current due to the reduction in the background charge carrier density. All these observations coherently point to the reduced trap density and background doping in the highly crystalline $EA_{0.08}$2D/3D film as the reason for the improved performance of the corresponding solar cells. The reduction in the non-radiative recombination of charge carriers contributes to the improvement of the V_{OC} of the $EA_{0.08}$2D/3D based HPSCs. The enhanced crystallographic order and morphological uniformity also have significant influence on the charge transport, in turn affecting the charge collection and recombination process in devices. The $EA_{0.08}$2D/3D film exhibits a better packing of the $FASnI_3$ grains in the out of plane direction, which yields lower disorder and scattering for charge transport. The enhanced charge collection further reduces the probability of charge recombination, leading to improvement in the J_{SC} and FF.

4. Conclusions

In conclusion, we demonstrate an effective way to enhance the device performance of tin perovskite solar cells. Adding EA cations into mixed 2D/3D films not only significantly improves the crystallinity and orientation of the 3D $FASnI_3$ grains, but also yields larger grains with compact and uniform film morphology. These changes lead to much lower trap density, background charge carrier density and charge recombination loss in EA_x2D/3D-based devices compared to devices based on pure mixed 2D/3D perovskites, which themselves were recently demonstrated to exhibit improved performance with respect to 3D $FASnI_3$. As a consequence, EA_x2D/3D-based devices exhibit much higher PCE and reproducibility compared to devices based on mixed 2D/3D perovskite films.

Acknowledgments

This work was financed through the Materials for Sustainability (Mat4Sus) programme (grant number 739.017.005) of the Netherlands Organisation for Scientific Research (NWO). This work is also part of the research program of the Foundation for Fundamental Research on Matter (FOM), which is part of the Netherlands Organisation for Scientific Research (NWO). This is a publication of the FOM-focus Group "Next Generation Organic Photovoltaics," participating in the Dutch Institute for Fundamental Energy Research (DIFFER). The authors would like to thank A. Kamp and T. Zaharia for technical support.

Appendix A. Supplementary data

Supplementary data to this article can be found online at https://doi.org/10.1016/j.nanoen.2019.04.040.

References

[1] https://www.nrel.gov/pv/cell-efficiency.html.
[2] A. Kojima, K. Teshima, Y. Shirai, T. Miyasaka, Organometal halide perovskites as visible-light sensitizers for photovoltaic cells, J. Am. Chem. Soc. 131 (2009) 6050–6051, https://doi.org/10.1021/ja809598r.
[3] M.M. Lee, J. Teuscher, T. Miyasaka, T.N. Murakami, H.J. Snaith, Efficient hybrid solar cells based on meso-superstructured organometal halide perovskites, Science 338 (2012) 643–647, https://doi.org/10.1126/science.1228604.
[4] J. Burschka, N. Pellet, S.-J. Moon, R. Humphry-Baker, P. Gao, M.K. Nazeeruddin, M. Grätzel, Sequential deposition as a route to high-performance perovskite-sensitized solar cells, Nature 499 (2013) 316–319, https://doi.org/10.1038/nature12340.
[5] N.J. Jeon, J.H. Noh, Y.C. Kim, W.S. Yang, S. Ryu, S. Il Seok, Solvent engineering for high-performance inorganic-organic hybrid perovskite solar cells, Nat. Mater. 13 (2014) 897–903, https://doi.org/10.1038/nmat4014.
[6] S. Shao, M. Abdu-Aguye, T.S. Sherkar, H.-H. Fang, S. Adjokatse, G. ten Brink, B.J. Kooi, L.J.A. Koster, M.A. Loi, The effect of the microstructure on trap-assisted recombination and light soaking phenomenon in hybrid perovskite solar cells, Adv. Funct. Mater. 26 (2016) 8094–8102, https://doi.org/10.1002/adfm.201602519.
[7] S. Shao, J. Liu, H.-H. Fang, L. Qiu, G.H. ten Brink, J.C. Hummelen, L.J.A. Koster, M.A. Loi, Efficient perovskite solar cells over a broad temperature window: the role of the charge carrier extraction, Adv. Energy Mater. 7 (2017) 1701305, https://doi.org/10.1002/aenm.201701305.
[8] K.P. Marshall, S. Tao, M. Walker, D.S. Cook, J. Lloyd-Hughes, S. Varagnolo,

A. Wijesekara, D. Walker, R.I. Walton, R.A. Hatton, Cs1 − xRbxSnI3 light harvesting semiconductors for perovskite photovoltaics, Mater. Chem. Front. 2 (2018) 1515–1522, https://doi.org/10.1039/C8QM00159F.

[9] M. Saliba, T. Matsui, J.-Y. Seo, K. Domanski, J.-P. Correa-Baena, M.K. Nazeeruddin, S.M. Zakeeruddin, W. Tress, A. Abate, A. Hagfeldt, M. Grätzel, Cesium-containing triple cation perovskite solar cells: improved stability, reproducibility and high efficiency, Energy Environ. Sci. 9 (2016) 1989–1997, https://doi.org/10.1039/C5EE03874J.

[10] M. Saliba, T. Matsui, K. Domanski, J.-Y. Seo, A. Ummadisingu, S.M. Zakeeruddin, J.-P. Correa-Baena, W.R. Tress, A. Abate, A. Hagfeldt, M. Grätzel, Incorporation of rubidium cations into perovskite solar cells improves photovoltaic performance, Science 80 (2016) 354, https://doi.org/10.1126/science.aah5557 206 LP-209.

[11] T. Singh, T. Miyasaka, Stabilizing the efficiency beyond 20% with a mixed cation perovskite solar cell fabricated in ambient air under controlled humidity, Adv. Energy Mater. 8 (2018) 1700677, https://doi.org/10.1002/aenm.201700677.

[12] T. Singh, S. Öz, A. Sasinska, R. Frohnhoven, S. Mathur, T. Miyasaka, Sulfate-assisted interfacial engineering for high yield and efficiency of triple cation perovskite solar cells with alkali-doped TiO2 electron-transporting layers, Adv. Funct. Mater. 28 (2018) 1706287, https://doi.org/10.1002/adfm.201706287.

[13] J. Chen, S.-G. Kim, N.-G. Park, FA0.88Cs0.12PbI3 − x(PF6)x interlayer formed by ion exchange reaction between perovskite and hole transporting layer for improving photovoltaic performance and stability, Adv. Mater. 30 (2018) 1801948, https://doi.org/10.1002/adma.201801948.

[14] A.H. Slavney, L. Leppert, D. Bartesaghi, A. Gold-Parker, M.F. Toney, T.J. Savenije, J.B. Neaton, H.I. Karunadasa, Defect-induced band-edge reconstruction of a bismuth-halide double perovskite for visible-light absorption, J. Am. Chem. Soc. 139 (2017) 5015–5018, https://doi.org/10.1021/jacs.7b01629.

[15] A. Filippetti, A. Mattoni, Hybrid perovskites for photovoltaics: insights from first principles, Phys. Rev. B 89 (2014) 125203, https://doi.org/10.1103/PhysRevB.89.125203.

[16] H.-H. Fang, S. Adjokatse, S. Shao, J. Even, M.A. Loi, Long-lived hot-carrier light emission and large blue shift in formamidinium tin triiodide perovskites, Nat. Commun. 9 (2018) 243, https://doi.org/10.1038/s41467-017-02684-w.

[17] J. Jiang, C.K. Onwudinanti, R.A. Hatton, P.A. Bobbert, S. Tao, Stabilizing lead-free all-inorganic tin halide perovskites by ion exchange, J. Phys. Chem. C. Nanomater. Interfaces. 122 (2018) 17660–17667, https://doi.org/10.1021/acs.jpcc.8b04013.

[18] N.K. Noel, S.D. Stranks, A. Abate, C. Wehrenfennig, S. Guarnera, A.-A. Haghighirad, A. Sadhanala, G.E. Eperon, S.K. Pathak, M.B. Johnston, A. Petrozza, L.M. Herz, H.J. Snaith, Lead-free organic-inorganic tin halide perovskites for photovoltaic applications, Energy Environ. Sci. 7 (2014) 3061–3068, https://doi.org/10.1039/C4EE01076K.

[19] S.J. Lee, S.S. Shin, Y.C. Kim, D. Kim, T.K. Ahn, J.H. Noh, J. Seo, S. Il Seok, Fabrication of efficient formamidinium tin iodide perovskite solar cells through SnF2–pyrazine complex, J. Am. Chem. Soc. 138 (2016) 3974–3977, https://doi.org/10.1021/jacs.6b00142.

[20] M.H. Kumar, S. Dharani, W.L. Leong, P.P. Boix, R.R. Prabhakar, T. Baikie, C. Shi, H. Ding, R. Ramesh, M. Asta, M. Graetzel, S.G. Mhaisalkar, N. Mathews, Lead-free halide perovskite solar cells with high photocurrents realized through vacancy modulation, Adv. Mater. 26 (2014) 7122–7127, https://doi.org/10.1002/adma.201401991.

[21] W. Liao, D. Zhao, Y. Yu, C.R. Grice, C. Wang, A.J. Cimaroli, P. Schulz, W. Meng, K. Zhu, R.-G. Xiong, Y. Yan, Lead-free inverted planar formamidinium tin triiodide perovskite solar cells achieving power conversion efficiencies up to 6.22%, Adv. Mater. 28 (2016) 9333–9340, https://doi.org/10.1002/adma.201602992.

[22] F. Wang, J. Ma, F. Xie, L. Li, J. Chen, J. Fan, N. Zhao, Organic cation-dependent degradation mechanism of organotin halide perovskites, Adv. Funct. Mater. 26 (2016) 3417–3423, https://doi.org/10.1002/adfm.201505127.

[23] S. Shao, J. Liu, G. Portale, H.-H. Fang, G.R. Blake, G.H. Brink, L.J.A. Koster, M.A. Loi, Highly reproducible Sn-based hybrid perovskite solar cells with 9% efficiency, Adv. Energy Mater 8 (2017) 1702019, https://doi.org/10.1002/aenm.201702019.

[24] W. Ke, C.C. Stoumpos, I. Spanopoulos, L. Mao, M. Chen, M.R. Wasielewski, M.G. Kanatzidis, Efficient Lead-Free Solar Cells Based on Hollow {en}MASnI3 Perovskites, J. Am. Chem. Soc. (2017), https://doi.org/10.1021/jacs.7b09018.

[25] F. Hao, C.C. Stoumpos, D.H. Cao, R.P.H. Chang, M.G. Kanatzidis, Lead-free solid-state organic–inorganic halide perovskite solar cells, Nat. Photon. 8 (2014) 489–494, https://doi.org/10.1038/nphoton.2014.82.

[26] H.-L. Hsu, C.-C. Chang, C.-P. Chen, B.-H. Jiang, R.-J. Jeng, C.-H. Cheng, High-performance and high-durability perovskite photovoltaic devices prepared using ethylammonium iodide as an additive, J. Mater. Chem. A. 3 (2015) 9271–9277, https://doi.org/10.1039/C5TA01563D.

[27] S.D. Stranks, V.M. Burlakov, T. Leijtens, J.M. Ball, A. Goriely, H.J. Snaith, Recombination kinetics in organic-inorganic perovskites: excitons, free charge, and subgap states, Phys. Rev. Appl. 2 (2014) 034007, , https://doi.org/10.1103/PhysRevApplied.2.034007.